Renewable Energy 180 (2021) 1300–1314

Contents lists available at ScienceDirect

Renewable Energy

journal homepage: www.elsevier.com/locate/renene

Design optimization of a novel vertical augmentation channel housing a cross-flow turbine and performance evaluation as a wave energy converter

A.H. Samitha Weerakoon [a, b], Byung-Ha Kim [b], Young-Jin Cho [b], Deepak Divashkar Prasad [c], M. Rafiuddin Ahmed [c], Young-Ho Lee [d, *]

[a] Department of Marine Engineering, Ocean University of Sri Lanka, Colombo 15, Sri Lanka
[b] Department of Mechanical Engineering, Graduate School, Korea Maritime and Ocean University, Busan, Republic of Korea
[c] Division of Mechanical Engineering, The University of the South Pacific, Suva, Fiji
[d] Division of Mechanical Engineering, College of Engineering, Korea Maritime and Ocean University, Busan, Republic of Korea

ARTICLE INFO

Article history:
Received 24 December 2020
Received in revised form
4 July 2021
Accepted 24 August 2021
Available online 10 September 2021

Keywords:
Wave energy
Oscillating water column (OWC)
Cross-flow turbine
Computational fluid
Dynamics (CFD)
Particle image velocimetry (PIV)
Augmentation channel

ABSTRACT

A novel vertical augmentation channel housing a direct-drive cross-flow turbine, with nozzles on both the sides of the turbine, was designed and an optimized configuration was obtained. The geometries of the guide nozzle and the front nozzle were optimized under steady flow conditions. The performance of the cross-flow turbine was analyzed using commercial computational fluid dynamics (CFD) code ANSYS-CFX. The optimized design was then evaluated as a wave energy converter both experimentally and computationally. The waves in the numerical wave tank (NWT) were generated using a piston type wave-maker. The optimized design gave a maximum output power of 13.2 W and an efficiency of 48.31% at a wave height of 0.2 m and wave period of 2.75 s for a rotational speed of 35 rpm. The difference between numerical and experimental efficiencies was within 3.5%. In addition to this, particle image velocimetry was used to study the flow characteristics in the augmentation channel and the turbine. The results show that the CFD code captures the flow in the augmentation channel and around the turbine accurately. The optimized design, which occupies less space than other wave energy converters, can be used to efficiently harness energy from the waves.

1. Introduction

The global energy consumption is steadily increasing and it is estimated that it will further increase by 30% or more by 2040 [1]. The primary reason for the rise in energy consumption is the increase in population. In addition to this, as economies grow, so do the electricity requirements. Most of the present energy demand is met by using fossil fuels and this trend does not appear to change in the near future. Greenhouse gas emissions are increasing as more fossil fuels are burnt. The increased concentrations of these gases trap more heat which results in global warming. The global averaged combined land and ocean surface temperature data shows an increase of 0.85 °C from 1880 to 2012 [2]. The excess heat leads to the melting of polar ice caps and glaciers which causes sea level rise. The impact of fossil fuels on the environment is devastating and this will continue unless clean energy sources are used for power production. A good solution is wave energy. Wave energy is environmentally friendly and non-emitting. Waves can be predicted well in advance and the energy flux is 15–20 times more than the wind or solar energy flux [3]. It is estimated that the global power potential of waves hitting the coasts worldwide is 1 TW [4].

The energy available in waves can be extracted using appropriate wave energy converters (WEC). WECs are generally categorized by the method used to capture the energy of the waves. The best known devices are point absorbers, attenuators, overtopping terminators and oscillating water column (OWC) devices. Amongst these, the OWCs are the most investigated WECs. OWC devices are generally equipped with air turbines namely Wells turbine, impulse turbine or Savonius turbine. Halder et al. [5] carried out numerical optimization of a Wells turbine. The blade sweep parameters at the tip and the mid-section were taken as the design variables. CFD

* Corresponding author.
E-mail addresses: SamithGT3@gmail.com (A.H.S. Weerakoon), lyh@kmou.ac.kr (Y.-H. Lee).

https://doi.org/10.1016/j.renene.2021.08.092
0960-1481/

Nomenclature

A	Amplitude (m)
A_{CS}	rear chamber cross-sectional area (m^2)
c_g	group velocity (m/s)
C_p	phase velocity (m/s)
E	wave energy (J/m^2)
g	acceleration due to gravity (m/s^2)
H	wave height (m)
h	water depth (m)
ΔH	head difference across the turbine (m)
k	wave number
N	rotations per minute (rpm)
Pr_{FN}	pressure in the front nozzle (Pa)
Pr_{RN}	pressure in the rear nozzle (Pa)
$P_{turbine}$	turbine power (W)
P_{water}	water power (W)
P_{wave}	wave energy flux (W/m)
Q	volume flow rate (m^3/s)
S	stroke of the piston (m)
T	wave period (s)
t	time-step (s)
W_G	guide nozzle width (m)
xdis	wave-maker displacement (m)
ΔY	rear chamber water level difference (m)
α	froude scale (−)
δ	nozzle entry arc angle (°)
η_t	turbine efficiency (−)
λ	wavelength (m)
ρ	water density (kg/m^3)
τ	Torque (N.m)
ω	angular velocity (rad/s)
ω_0	frequency (Hz)

simulations showed that the peak torque coefficient increased by 28.3% but the corresponding efficiency decreased by 13.5% due to adverse flow conditions. In another study on Wells turbine by Halder et al. [6], the authors reported that for the optimal design, the relative power and the relative stall point increased by 29% and 18% respectively when compared to the base model. The effect of guide vane shape was investigated by Abdulhadi [7]. The study highlighted the superior performance of the turbine using three-dimensional guide vanes compared to two-dimensional guide vanes. The maximum efficiency for the design with three-dimensional guide vanes was 1.1% higher than that with two-dimensional guide vanes. Badhurshah et al. [8] numerically investigated the performance of an impulse turbine with fixed guide vanes. The authors highlighted an increase in the pressure gradient with increasing turbine speed. With increasing turbine speed, the separation point of the vortex formation moved towards the blade hub. Furthermore, increasing the turbine speed increased the peak suction on the suction side causing the flow to separate near the trailing edge of the blade. Luo et al. [9] numerically studied the performance of an axial impulse turbine. They varied the number of guide vanes, the guide vane type, the gap between the guide vane and the blade, and hub to tip ratio. The authors highlighted that the hub to tip ratio has a strong influence on turbine performance. A thorough review of air turbines used in OWCs can be found in references [10,11].

Though air turbines are extensively used in OWCs, there are problems such as high rotational variability and aerodynamic losses induced by the noise coming from the turbine passage at extreme sea conditions [12]. To address these problems, researchers are proposing the use of direct-drive turbines (DDT). In a DDT, the wave energy is directly converted to mechanical energy by the turbine. It eliminates the wave energy to pneumatic energy conversion since water directly drives the turbine similar to a hydro-turbine. Prasad et al. [12] numerically investigated the performance of a cross-flow turbine used as a DDT for wave energy applications at different wave conditions and varying turbine speeds. The authors reported a peak efficiency of 55%. In another study by Prasad et al. [13], the authors investigated the performance of a cross-flow turbine numerically. The turbine speed was varied at a fixed wave height of 0.2 m and a wave period of 2.0 s. The authors reported a peak efficiency of 44.73% at a turbine speed of 35 rpm. Choi et al. [14] investigated the performance of a cross-flow turbine integrated with a caisson both experimentally and numerically. The peak efficiency reported in the study was 48.6%. The influence of attachments to a cross-flow turbine and its performance was reported by Choi et al. [15]. The performance of a novel floating type WEC was reported by Kim et al. [16]. The device had two water column chambers on either side of the augmentation channel which housed a cross-flow turbine. Performance studies showed a peak efficiency in the range of 35%–45%. Akimoto et al. [17] designed and tested a drag-type cross-water water turbne for extracting energy from the orbital fluid motion in ocean waves. A thorough review of the modeling of different types of wave energy systems in numerical wave tanks was performed by Windt et al. [18].

A cross-flow turbine is essentially an impulse turbine. It can handle large quantities of water and also possesses flat efficiency characteristics. In this type of turbine, the water passes over the blades twice, resulting in a higher momentum transfer. A review of the literature shows limited amount of information on the use of cross-flow turbines for wave power applications. In addition to this, the existing devices use horizontally configured augmentation channels in which the turbine is housed and the flow takes place in the horizontal direction. The present study not only looks at using the cross-flow turbine for wave power applications but also proposes a new vertically configured augmentation channel through which the water flows vertically in and out due to wave action. Thus, the flow at the inlet, at the outlet and through the turbine is in the vertical direction. This makes the design compact and the whole WEC occupies less space. The turbine is fully submerged in water and under the action of incoming waves generates power bi-directionally while rotating in just one direction. The present study includes both experimental and computational works.

The experimental work was carried out in the wave channel at Korea Maritime and Ocean University and the numerical work was performed using commercial CFD code ANSYS-CFX R19 [19]. The waves in the numerical wave tank (NWT) were generated using a piston-type wave-maker and the free surface was captured using VOF method. Initially, the geometry of the attachments (the augmentation channel) was optimized using steady flow conditions. The optimized model was then fabricated and experimentally tested as a wave energy converter (WEC) at different wave conditions in the second part of the work. Results were obtained from the CFD code under transient conditions and these results were compared against the experimental results. Finally, experiments were conducted at different wave heights, water depths and wave periods and the conditions at wich high efficiencies were obtained are presented.

2. Methodology

2.1. Numerical method

The geometry of the augmentation channel is shown in Fig. 1. The augmentation channel consists of a front nozzle, a rear nozzle and the turbine. Both the front and the rear nozzles guide the flow smoothly onto the turbine blades. The flow through the guide nozzle which receives the waves in the horizontal direction, is redirected vertically through the front nozzle. The turbine is positioned right above the front nozzle. The overall height, length and width of the model are 1704 mm, 1232 mm and 700 mm respectively. The guide nozzle is 800 mm high, 722 mm long and 700 mm wide and has a 45–degree inlet angle with respect to the horizontal plane. The dimensions of the turbine blades are also shown in Fig. 1. The design and shape of the blades were adopted using the previous works of the same authors [20,21]. The turbine has an outer diameter of 260 mm, an inner diameter of 165 mm and a width of 700 mm. The turbine has a total of 30 blades; the blade entry angle is 30° and the exit angle is 90°. Each blade is 3 mm thick, as shown in Fig. 1.

The grid generation was accomplished using ANSYS ICEM CFD. The whole model was divided into four parts, as shown in Fig. 2. The model used for steady flow analysis had approximately 1.86 million nodes while the model for transient analysis had approximately 1.99 million nodes [21]. The major difference between the two models is the moving mesh region that is present in the transient analysis. The obtained y+ was kept the same as previous studies [20]. The $y+$ for the different parts were: $y+ < 10$ (turbine), $y+ < 50$ (nozzle and chamber). The boundary conditions used for steady and transient analysis are shown in Fig. 3 and Table 1. The steady flow analysis was performed using single-phase flow (water). For the steady flow case, a static pressure of 3 kPa was specified at the inlet of the pipe whose length was five times the diameter of the turbine. The outlet was assigned as an opening with a relative pressure set to 0 Pa. The rest of the exterior walls and the turbine blades were modeled as walls with no-slip boundary conditions. The domain interfaces were connected using automatic mesh connection method. The RMS residual limit was set to 10^{-6} to achieve better convergence of the solutions. A mesh independence test was carried out to study the effect of number of nodes on the turbine's power and efficiency at 50 rpm for steady flow conditions. It was found that at 1.35 million nodes, the turbine power was 16.17 W and the efficiency was 45.54%. When the number of nodes were increased to 1.86 million, the power was 15.64 W and the efficiency was 44.07%. When the number of nodes was further increased to 2.03 million, the power was 15.62 W and the efficiency was 44.02%. Hence, it was decided to carry out all the steady flow simulations at 1.86 million nodes, since a further increase only results in more computing time without any significant change in the output parameters.

For the transient analysis (wave energy conversion), multiphase simulation (water and air) was used and the air-water free surface was captured using the VOF method [22]. The wave-maker was modeled as a moving wall. The sinusoidal displacement of the wave-maker in the x-direction was defined as a function of time by equation (1)

$$x_{dis} = S \times \sin(\omega_0 \times t) \tag{1}$$

where S is the stroke, ω_0 is the frequency and t is the simulation time-step. The relation between the stroke of the piston and the wave height is given by equation (2) [20].

$$\frac{H}{S} = \frac{2[\cosh(2kh) - 1]}{\sinh 2kh + 2kh} \tag{2}$$

The top wall of the NWT and the chamber outlet were modeled as openings. Similar to steady flow analysis, the rest of the exterior walls and the turbine blades were modeled as walls with no-slip boundary condition. The domain interfaces were appropriately connected using the automatic mesh connection method. The total flow time for the transient simulation was set to 60 s with a time step of 0.01 s. All the domains for the steady and transient analyses were stationary except for the turbine domain. The turbine domain was a rotating domain with user-specified speeds. The simulation was performed based on Reynolds averaged Navier–Stokes (RANS) equations with closure provided by the SST (Shear-Stress-Transport) turbulence model. The time discretization of the equations was achieved with the implicit second-order Backward Euler scheme [23,24].

2.2. Experimental method

The experimental setup and wave tank used in the present work are shown in Fig. 4 (a) and Fig. 4 (b) respectively. The wave tank has a length of 7.3 m, a height of 1.8 m and a width of 1.0 m. Pressure

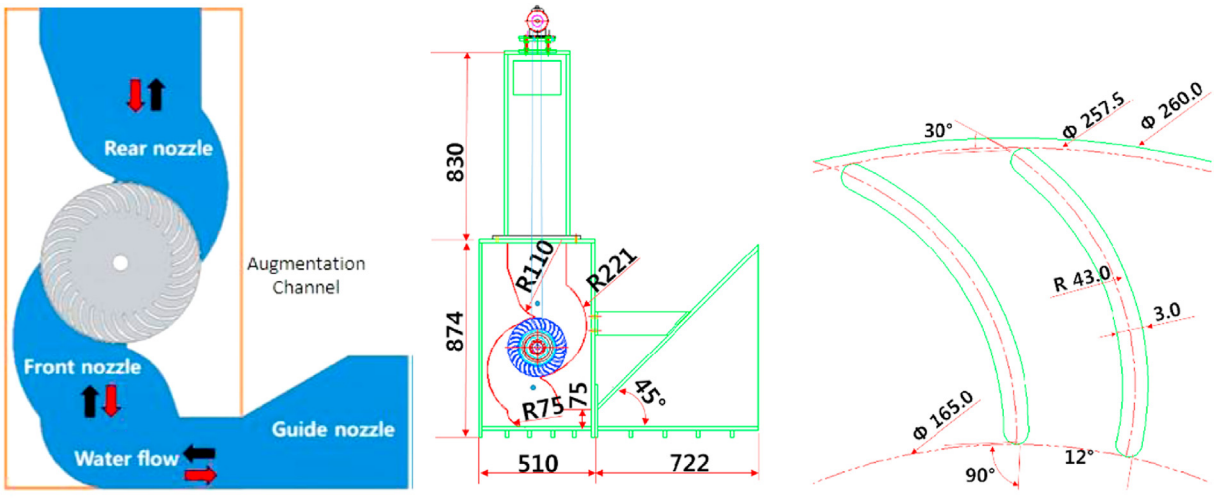

Fig. 1. Schematic of the vertical augmentation channel and the turbine blade.

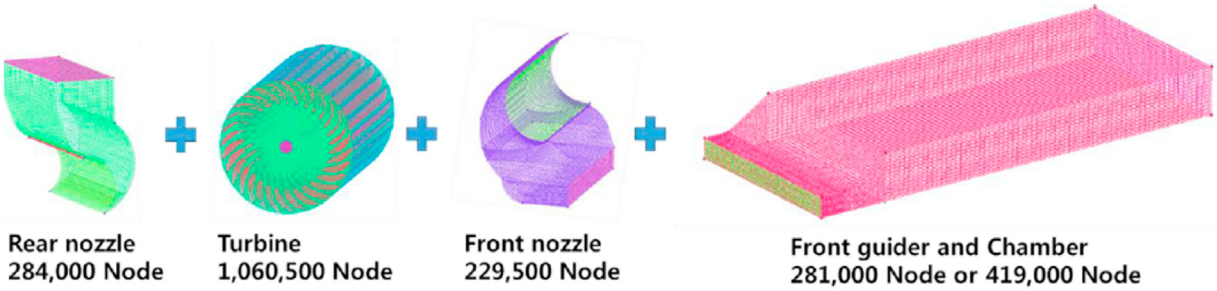

Fig. 2. Grid generation details.

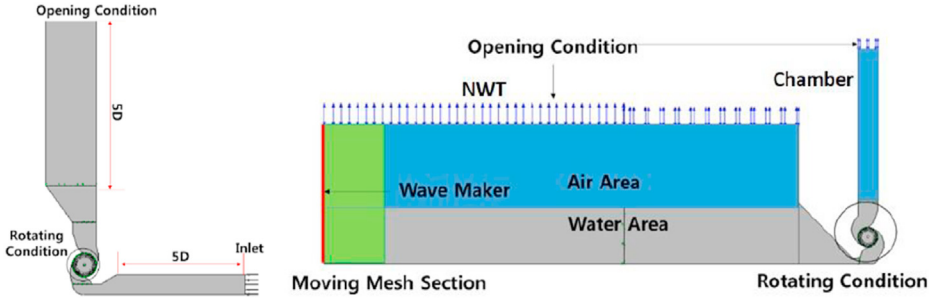

Fig. 3. The numerical models and the boundary conditions for steady flow analysis (left) and transient analysis (right).

Table 1
Boundary conditions for the two simulations.

Simulation Type	Steady flow	Transient
Mesh Type	Hexahedral	Hexahedral
No. of Nodes	1.86×10^6	1.99×10^6
Time	Steady flow (Time averaged)	Transient (60 Seconds)
Turbulence Model	Shear Stress Transport (SST)	Shear Stress Transport (SST)
Fluid Phase	Single Phase (Water)	2 Phase (Water and Air)
Mesh Motion	–	Moving
Outlet	Opening	Opening
Rotational Speed	20, 30, 40, 50, 60, 70 and 80 rpm	20, 25 and 30 rpm
Rotor Stator Interface	Frozen Rotor	Transient Rotor Stator

measurements were performed with the help of pressure taps by drilling holes on the top and bottom of the rear nozzle and front nozzle of the augmentation channel, as shown n Fig. 5. The actual wave measurement data near the korea maritime and ocean university (KMOU), South Korea, as shown in Fig. 6 were converted using Froude scaling ($\alpha = 5$) to obtain the experimental wave conditions as given in Table 2. The experimental model shown in Fig. 1 was constructed to a scale of 1:5 using a 10 mm thick acrylic sheet as shown in Fig. 7 (a). It is generally accepted that larger models reduce scaling effects. However, the scale ratio chosen was strongly dictated by the physical dimensions of the wave tank and the wave generating capabilities [25]. The desired waves were generated by controlling the stroke and speed of the piston. The turbine was installed at the back of the wave tank. A sloping beach which consisted of multiple porous plates of different porosity levels was placed at the rear end of the channel to reduce the reflection of waves. At the top of the chamber, a torque transducer, rpm sensor and a power brake were used to measure the turbine speed and torque.

The torque transducer was connected to the turbine using a belt drive system having a ratio of 1:1 [26]. The torque transducer (model – YDR-2K) is capable of measuring up to 19.61 N-m of torque with an accuracy of 0.09% and a repeatability of ±0.3%. The speed of the turbine was measured using an internally inserted ONO SOKKI MP-981 magnetic type detector that has a measurement range of 1–20,000 rpm. The tachometer has an accuracy of 0.01% and a resolution of ±1 rpm. A PORA power brake (model PRB-Y3) was used for controlling the rotational speed of the turbine. General Acoustics UltraLab® ULS sensor, model USS20130, with a resolution of 0.36 mm and a measurement range of 200 to 1300 mm was used for measuring the wave height and the water oscillations in the chamber. The pressure transducer (model DWSD0020R1AA) was able to measure differential pressure in the range of 0–20 kPa with an accuracy of 0.075%. The digital signals from all the sensors were stored at the same time using a data-logger (model PT-1624). PIV measurements were performed to investigate the flow characteristics in the augmentation channel as well as around the turbine as shown in Fig. 7 (a) and Fig. 7 (b). The tracer particles used were polyvinyl chloride (PVC) with a specific gravity of 1.02 and an average particle diameter of 100 μm. The particles were illuminated using an air-cooled diode pumped solid-state laser of 4 W power. A high speed camera (UX50) was used to capture the motion of the seeded PVC particles. The camera was set to capture 500 frames per second for 60 s with an image resolution of 1024 x 768 pixels. Cactus 3.3 software was used to post-process the images. To get an accurate estimate of the error in PIV

a.

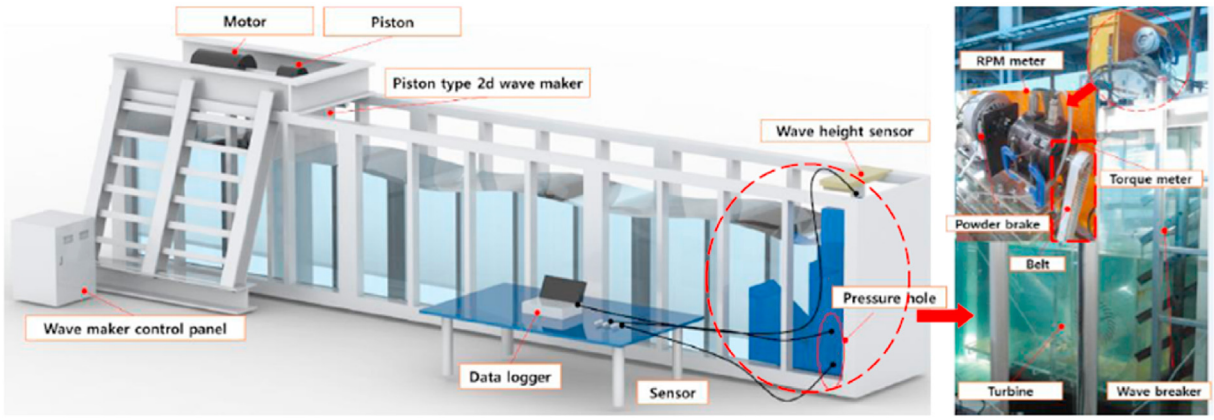

b.

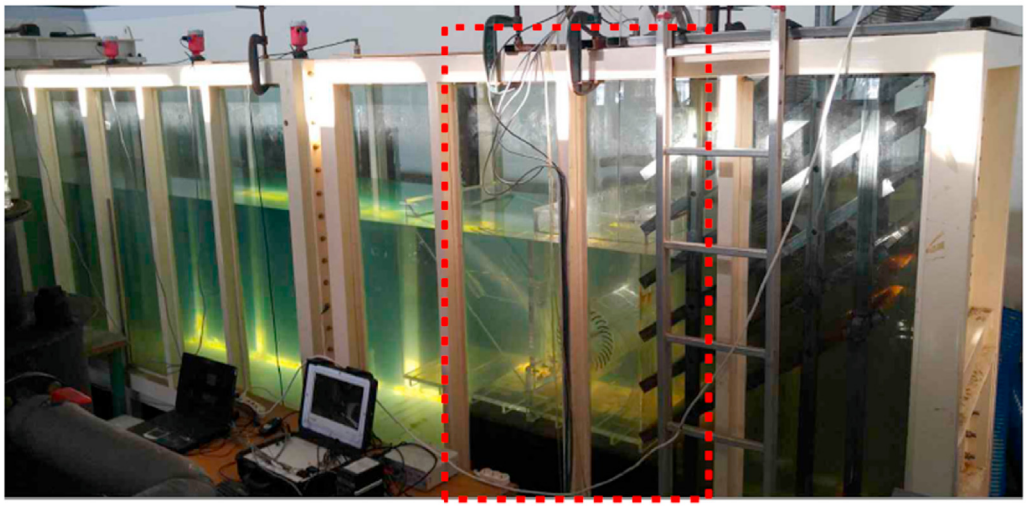

Fig. 4. (a) Experimental setup (b) wave tank.

measurements, PIV measurements were performed on a calibrated, constant speed rotating motion and the maximum error was found to be 0.32%.

3. Results and discussion

3.1. Geometric optimization

Geometric optimization was carried out computationally to ensure that the turbine setup is optimized for best performance. Equations (3)–(7) [27,28] were used to obtain water power, shaft power and turbine efficiency. The values used were averaged over 10 s. The water density (ρ) was 998 kg/m^3 and acceleration due to gravity (g) was 9.81 m/s^2. The cross-sectional area of the chamber (A_{CS}) was 0.182 m^2.

$$P_{water} = \rho g Q \Delta H \tag{3}$$

$$\text{where } \Delta H = \frac{\text{Pr}_{RN} - \text{Pr}_{FN}}{\rho g} \tag{4}$$

$$\text{and } Q = \frac{2A_{CS}\Delta Y}{T} \tag{5}$$

$$P_{turbine} = \tau \times \omega \tag{6}$$

$$\eta = \frac{P_{turbine}}{P_{water}} \tag{7}$$

Optimization was done using steady flow analysis due to the reason that it reduces the simulation time significantly when compared to transient simulation. The nozzle entry arc angle δ shown in Fig. 8, was optimized first. It was varied from 90° to 150° in increments of 20°. It is clear from the graph in Fig. 8 that the best performance was obtained for a 150° entry arc angle with a peak efficiency of 38.58% achieved at 50 rpm. The poorest performance was observed for the 90° arc angle with a peak efficiency of 31.6%. By having a larger entry angle, more blades directly receive the incoming flow and as a result, more energy is transferred to the blades as shown in Fig. 9. This results in higher power production while keeping the inlet conditions same. The 150° entry arc angle model, which will be called the base model henceforth, is used for further optimization.

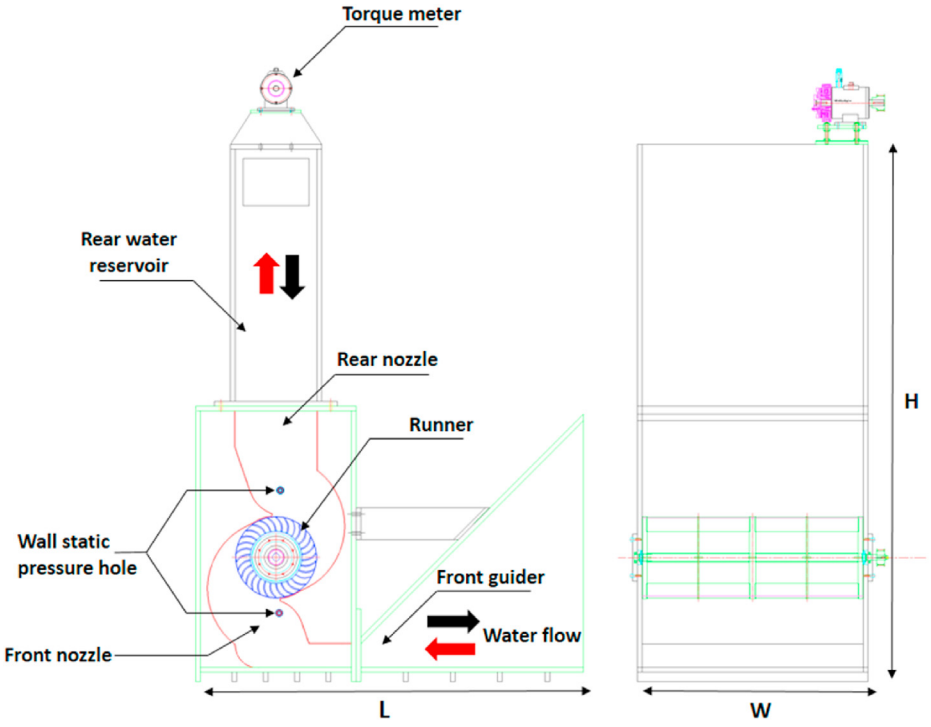

Fig. 5. Wall static pressure holes on the augmentation channel.

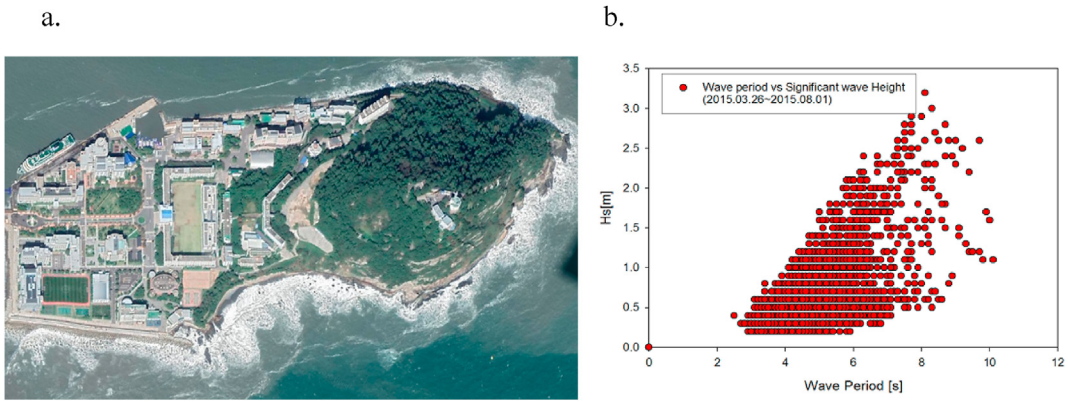

Fig. 6. Wave observation point and wave measurement results. (a) Map of korea maritime and ocean university. (b) Wave period vs. wave height.

Table 2
Field wave height and wave period and corresponding experimental values obtained using Froude scaling.

Wave height (m)			Wave Period (s)		
Physical Qty	Field (Hf)	Exp. (Hf/α)	Physical Qty	Field (Tf)	Exp. (Tf/α1/2)
H1	0.75	0.15	T1	4.47	2.00
H2	1.00	0.2	T2	5.03	2.25
H3	1.25	0.25	T3	5.6	2.50
			T4	6.15	2.75

The parameters A, B, C and D, shown in Fig. 10 were then optimized keeping the above-mentioned base model entry arc angle of 150° constant.

The front guide shape was optimized first – the effect of front guide shape on the turbine performance was investigated using 3 different configurations; namely: 45° inclined (D1), 30° inclined (D2) and ball-mouse (D3). As illustrated in Fig. 11, turbine efficiencies for the different front guide configurations are peak at 50 rpm. The streamlines for the 3 cases, shown in Fig. 12, indicate greater flow rate into the rotor and hence higher energy transfer for the 45° inclined orientation compared to the other 2 cases. As observed by NWT CFD results and PIV measurements (Fig. 23 and Fig. 24), there is a small re-circulation zone near the front wall of the nozzle without any noticeable difference in all 3 cases, but this

a.

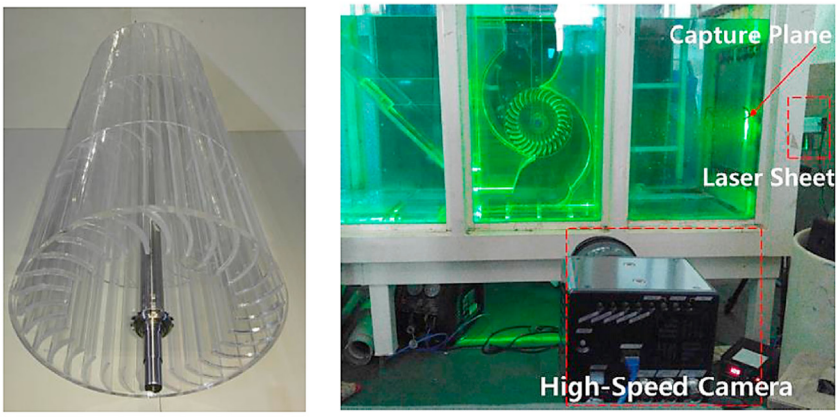

b.

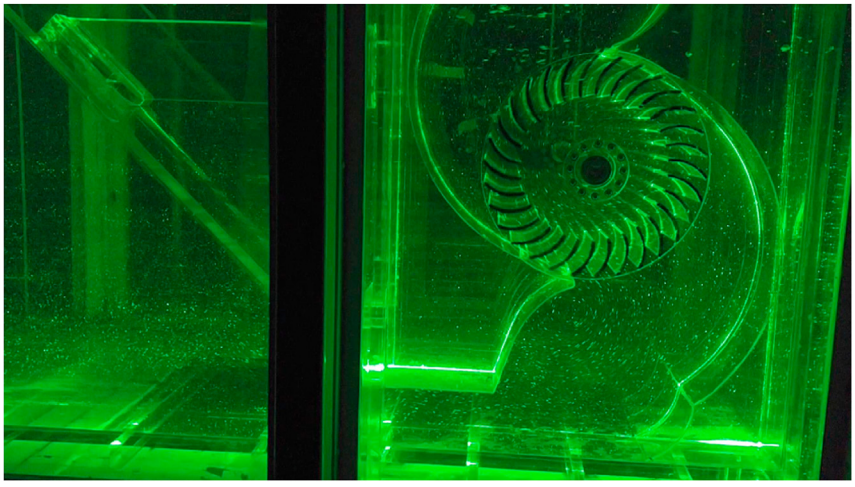

Fig. 7. (a) A photograph of the cross-flow turbine and PIV measurements in the setup. (b) A photograph of the cross-flow turbine during the experiment.

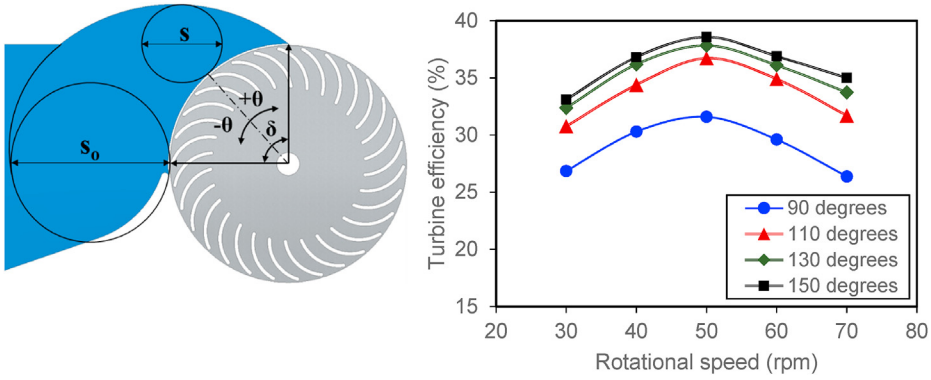

Fig. 8. Schematic of the nozzle entry arc angle (left) and Turbine efficiency at varying speed for different entry arc angles (right).

re-circulation zone did not affect the main flow towards the blades. The front guide shape does not influence the turbine performance significantly at a given rpm. The turbine efficiency peaked at 39.75% at 50 rpm for the 45° model with a 0.47% difference compared to the 30° model.

Two upper-wall nozzle shape configurations were tested; curved upper-wall (C1) and straight upper-wall (C2). The streamlines for the two configurations at the rotational speed of 50 rpm are shown in Fig. 13. It is observed that the region J has a re-circulating flow for both the models; however, the flow directed towards the blades shows higher flow of water and hence more energy transfer at the specified blade inlet angle for the curved upper-wall model. The streamlines clearly show a higher mass flow directed towards the rotor. The curved upper-wall model performs better than the straight upper-wall model at the peak efficiency point of 50 rpm, as shown in Fig. 14. The peak efficiency is approximately 40% at 50 rpm, which decreases considerably from this point onwards. On an average, the efficiency for the curved

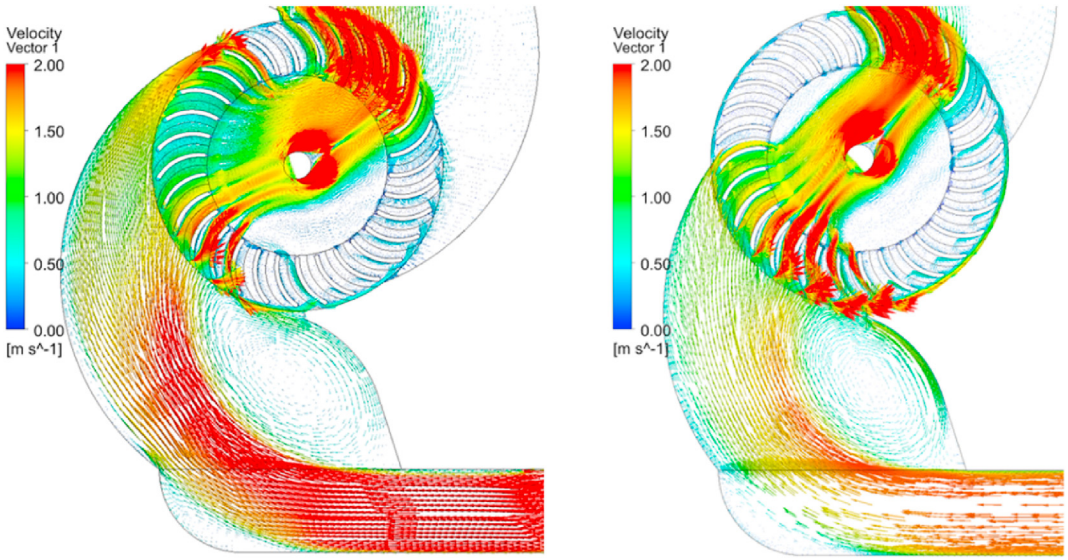

Fig. 9. Velocity vectors for the 150° and 90° entry arc angles.

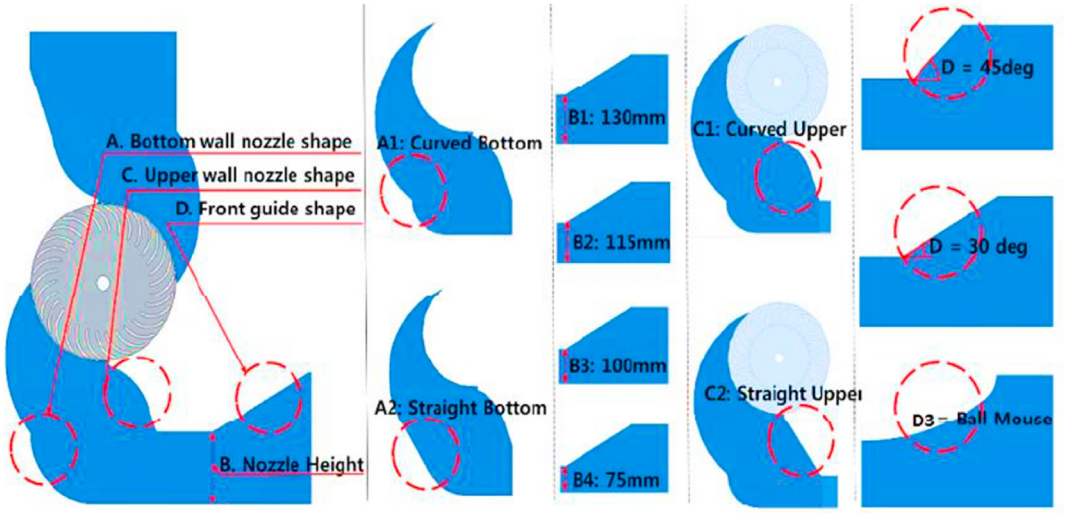

Fig. 10. Design configurations of the base model (A) and modification parameters (B).

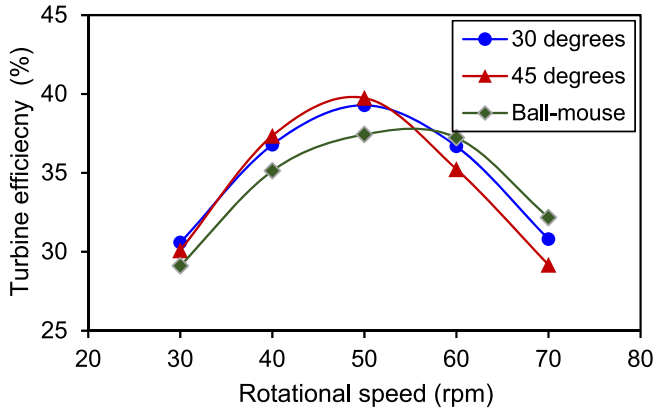

Fig. 11. Effect of front guide upper wall shape on the turbine efficiency at different rotational speeds.

upper-wall model is 0.5% higher than that recorded for the straight upper-wall model. It can be noted that the flow velocity in the region J of Fig. 13 is considerably small compared to the velocity through the main region which enters the turbine blades at the optimum angle; for this reason, the effect of changing the shape of the upper wall did not have a significant effect on the efficiency of the turbine. The curved upper-wall model was further optimized as described below.

Four different nozzle height configurations (section B in Fig. 10) were simulated to investigate their effect on turbine performance. The efficiencies at different rotational speeds are shown in Fig. 14. The nozzle with a height of 75 mm performed the best at all the rotational speeds of 30–70 rpm. Thus, the nozzle height has a significant effect on the novel vertical turbine performance. The peak efficiency of approximately 40% is achieved at 50 rpm; the efficiency then decreases significantly from this point onwards.

At 50 rpm, the efficiency of the 75 mm nozzle improved significantly compared to the other nozzle heights, mainly due to an increase in velocity of the fluid compared to the other 3 cases. A

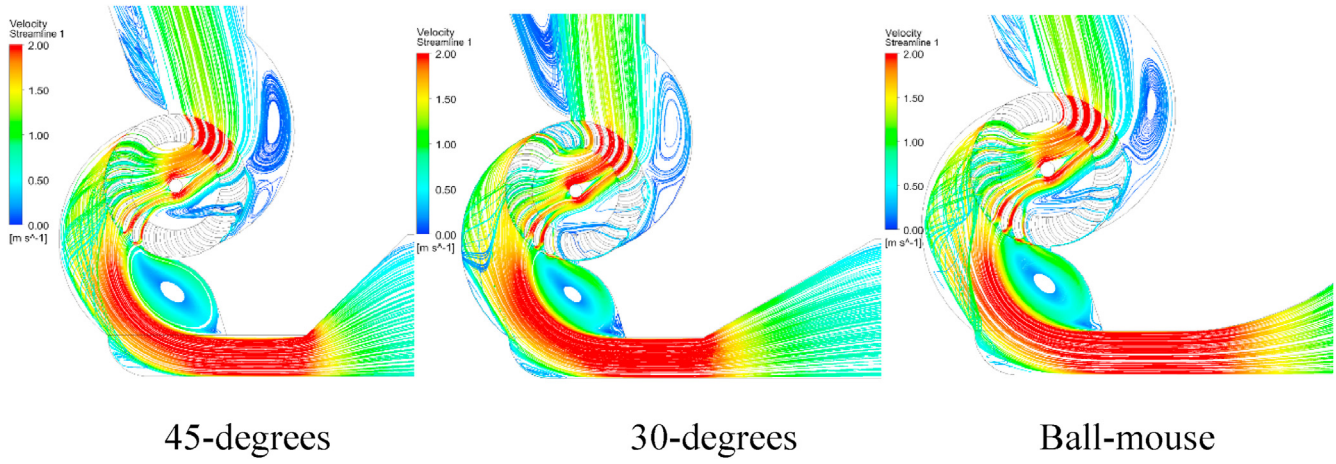

Fig. 12. Streamlines for different front guide nozzle configurations at 50 rpm.

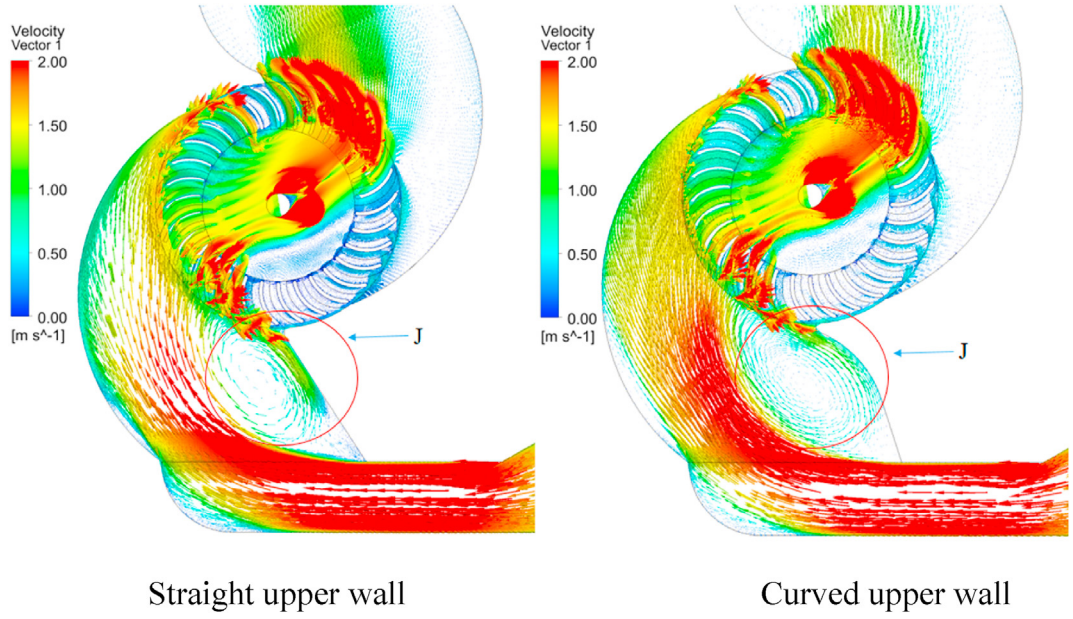

Fig. 13. Streamline for the two upper-wall nozzle shape configurations at 50 rpm.

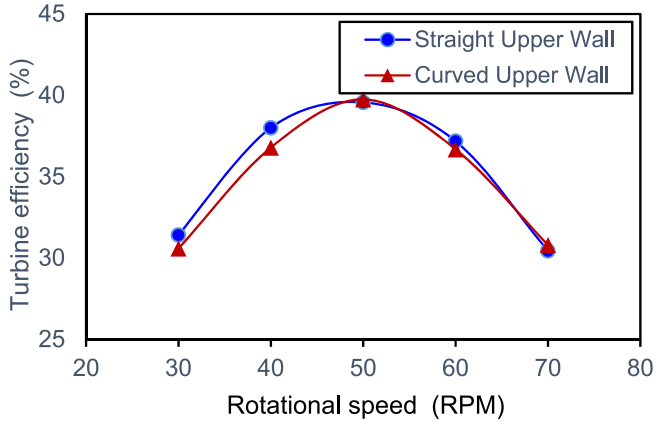

Fig. 14. Effect of upper-wall nozzle shape on the turbine efficiency.

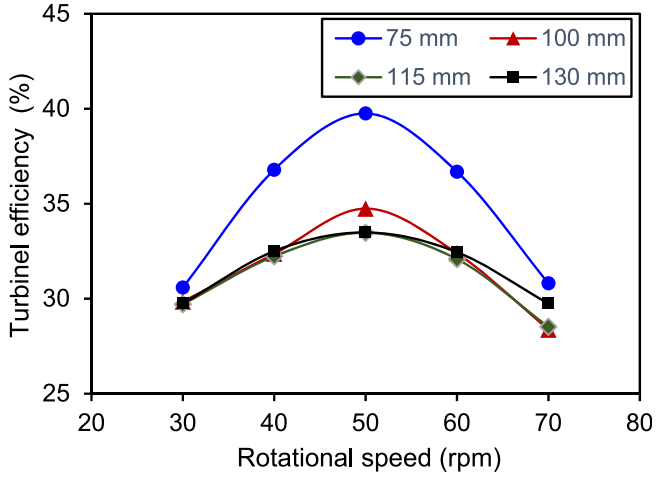

Fig. 15. Effect of nozzle height on turbine efficiency at different rotational speeds.

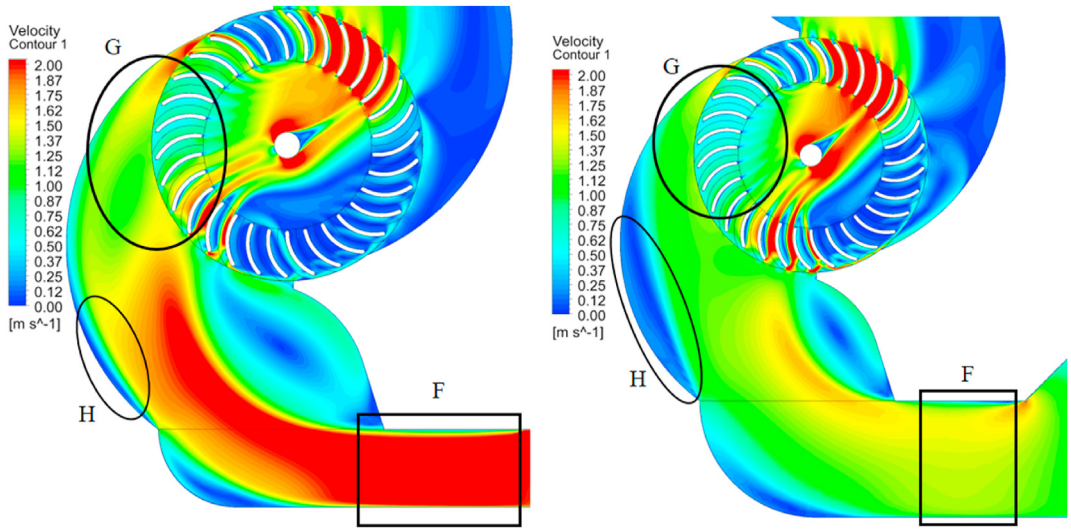

Fig. 16. Velocity contour plots for the 75 mm and 130 mm nozzle configurations at 50 rpm.

higher percentage of pressure energy is being converted into kinetic energy of the fluid stream when passing through the 75 mm nozzle. The streamlines for the nozzle heights of 75 mm and 130 mm at the rotational speed of 50 rpm are shown in Fig. 16. It is clear from the figure that better flow characteristics are observed for the 75 mm model. Firstly, the velocity recorded in region F for the 75 mm model is much higher than that recorded for the 130 mm model. For the 75 mm nozzle, the velocity ranges from 1.5 to 2.0 m/s in region F while for the 130 mm nozzle, it ranged from 1.0 to 1.5 m/s. The higher energy transport recorded for the 75 mm model in region F ultimately leads to higher energy availability observed in region G, resulting in more energy transfer to the turbine blades and hence higher power generation. This higher energy transfer increases the turbine efficiency as seen in Fig. 15. The region H, for the 75 mm nozzle shows almost zero flow re-circulation compared to the 130 mm segment showing greater re-circulation. As a consequence, a much wider and high energy density is available on the runner blades, hence an increase in the power output and the efficiency compared to the 130 mm nozzle height. It is also interesting to identify a wider fluid column remain attached to the outer wall of the curved nozzle periphery on the 75 mm setup making the fluid path strike the turbine blades at the desired entry angle, imparting more torque than the 130 mm nozzle. However, this reduction in nozzle height caused about 5% reduction in the flow rate. Any further reduction in the nozzle height would have increased the resistance to flow and would have resulted in a significantly lower energy available at the turbine inlet; hence, it was not reduced further. The 75 mm model was further optimized.

Two bottom-wall nozzle shape configurations were tested. The base model had a curved bottom-wall (A1) while the other had a straight bottom-wall (A2). The streamlines and the velocity vectors for the two configurations at the turbine rotational speed of 50 rpm are shown in Fig. 17. It is observed that the re-circulating flow in region A for the straight bottom-wall model is eliminated. However; interestingly, better flow characteristics with higher kinetic energy are observed for the curved bottom-wall model at the blade inlet region (E). As a result of this, the curved bottom-wall model performs better than the straight bottom-wall model at the turbine speed of 50 rpm, as shown in Fig. 18. The peak efficiency of 44.07% is recorded at 50 rpm for the curved bottom-wall model. The curved (A1) design provides a better path for the water stream entering the curved bottom wall guide from the 75 mm (B4) height front nozzle. The efficiency of the curved bottom wall model was about 1% higher than that recorded for the straight bottom-wall model at the rotational speed of 50 rpm.

After completing the optimization work using steady flow analysis, it was observed that the optimum performance for all the best configurations always occurred at a rotational speed of 50 rpm. The power output and the efficiency of the optimized design are 15.64 W and 44.07% respectively, with an increase of 5.5% in the efficiency compared to the base model, which is a considerable improvement. The findings from the above work indicate that the performance of the turbine at fixed flow conditions can be improved by optimizing the various components of the augmentation channel which is on both sides of the turbine. Acharya et al. [29] modified the rear nozzle wall, adjusted the guide vane opening and changed the number of blades of the reference turbine. The authors reported that the efficiency increased from 63% to 76% from their work. The effect of solidity on turbine performance was reported by Totapally and Aziz [30]. The authors highlighted that an efficiency of 90% could be achieved by just changing the number of blades from 30 to 35. Chen et al. [31] highlighted that the efficiency of a cross-flow turbine can be improved by 12.5% by using well shaped nozzle at the inlet. Adhikari and Wood [32] also studied the influence of nozzle shape on turbine performance. More information on geometric modifications to improve the performance of a cross-flow turbine can be found in references [33–36]. Elbatran et al. [37] tested a new configuration with bi-directional nozzles and twin cross-flow turbines and achieved a maximum efficiency of 52%. Mehr et al. [38] carried out an optimization study of a cross-flow turbine; they optimized the nozzle geometry and angle of attack followed by turbine parameters to achieve a high efficiency.

3.2. Wave tank experiments

The optimized design, obtained from steady flow analysis, was then constructed for experimental work in the wave tank shown in Fig. 7 (a) and for CFD simulations in the NWT shown in Fig. 3. The experiments were conducted for the parameters given in Table 2. In addition to this, the experiments were also conducted at the water depths (h) of 0.7 m, 0.8 m, 1.0 m and 1.1 m. Turbine power and efficiency were calculated using equations (8)–(13) [27,28]. In the following equations, C_p, c_g and W_G are phase velocity, group velocity

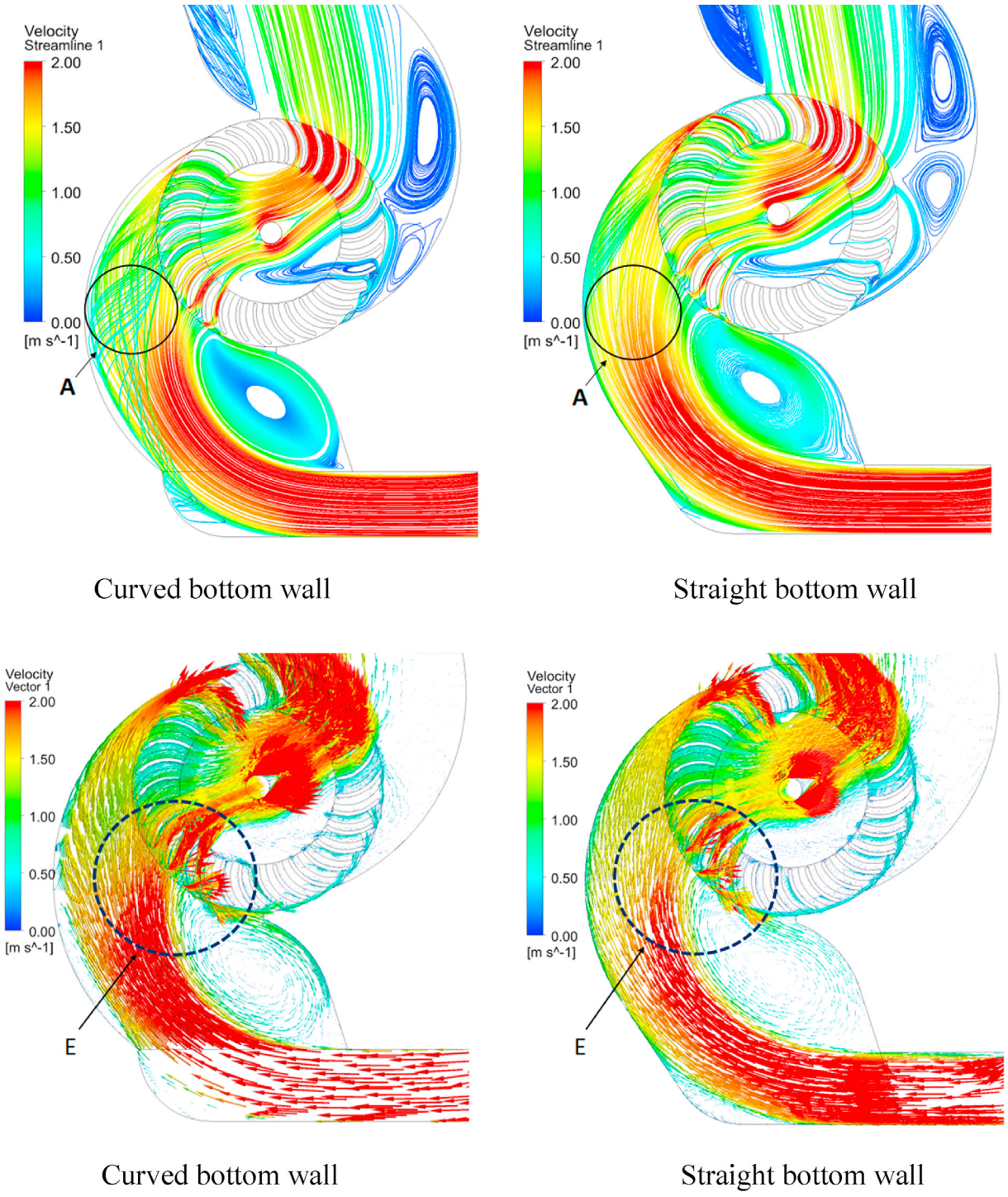

Fig. 17. Streamlines and velocity vectors for the two bottom-wall nozzle shapes at the rotational speed of 50 rpm.

and guide nozzle width respectively.

$$C_p = \sqrt{\frac{g\lambda}{2\pi}\tanh\left(\frac{2\pi h}{\lambda}\right)} \quad (8)$$

$$c_g = \frac{1}{2}C_p\left\{1+\frac{4\pi h}{\lambda}\left(\frac{1}{\sinh\left(4\pi h/\lambda\right)}\right)\right\} \quad (9)$$

$$P_{wave} = Ec_g\ ;\ \left\{where; E = \frac{1}{8}\rho g H^2\right\} \quad (10)$$

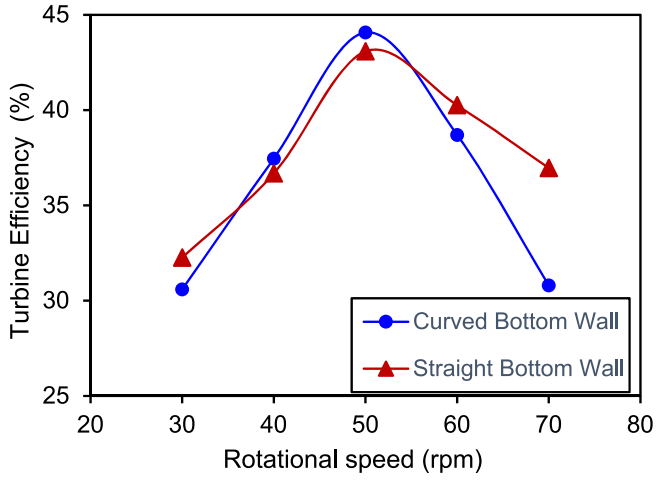

Fig. 18. Effect of bottom wall nozzle shape on the turbine's efficiency.

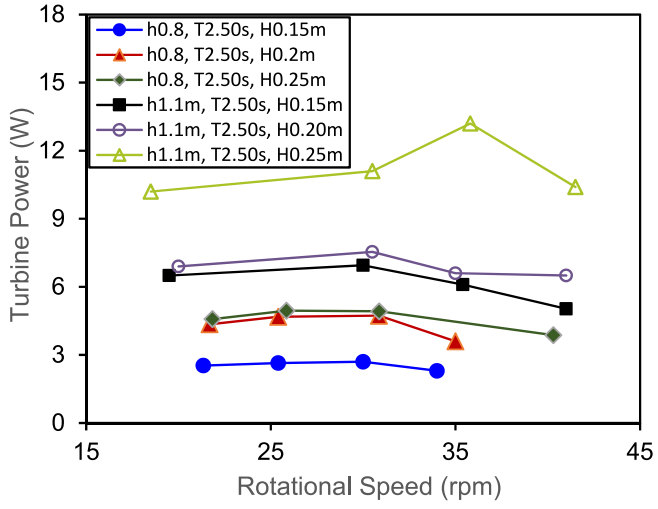

Fig. 19. Turbine power at different wave heights and water depths for a wave period of 2.5 s.

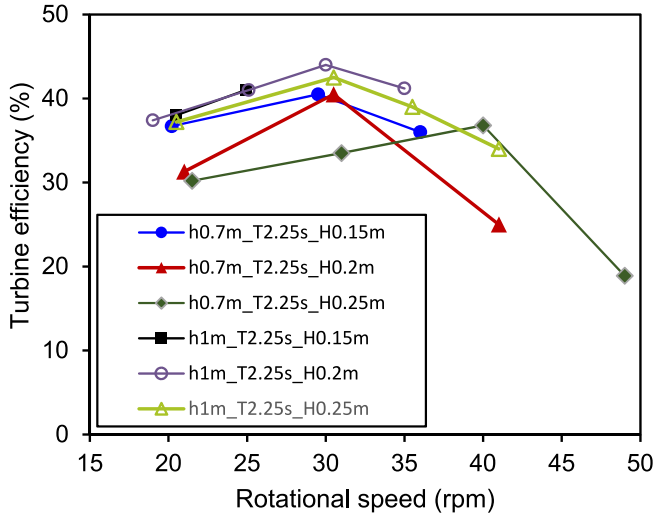

Fig. 20. Turbine efficiency at different wave heights and water depths for a wave period of 2.25 s.

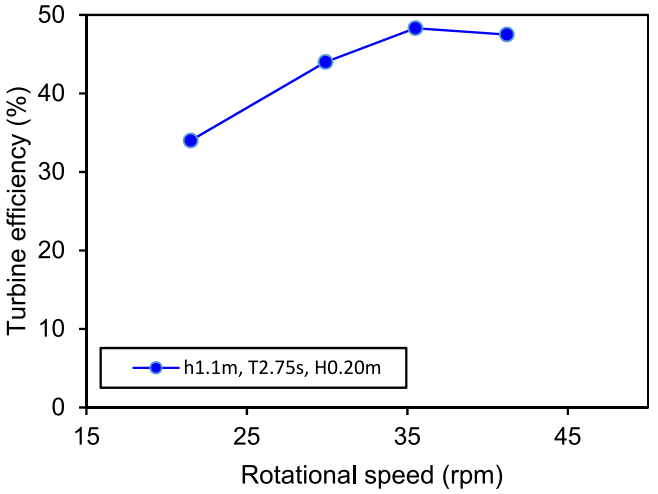

Fig. 21. Turbine efficiency at a water depth of 1.1 m, a wave height of 0.2 m and for a wave period of 2.25 s.

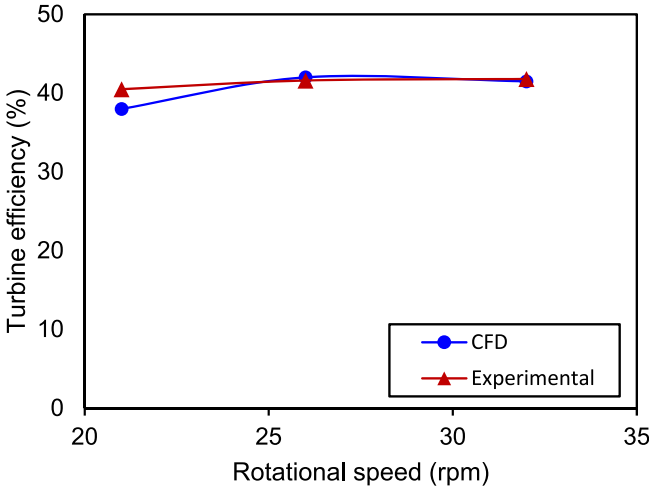

Fig. 22. Comparison of turbine's efficiency obtained through CFD and experiments.

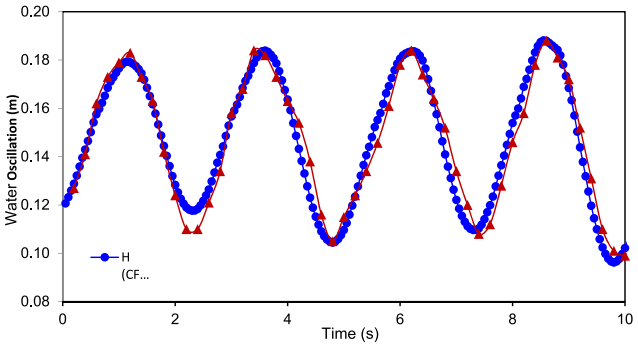

Fig. 23. Comparison of computational and experimental water oscillations in the chamber.

$$P_{wave} = \frac{1}{8}\rho g H^2 c_g \tag{11}$$

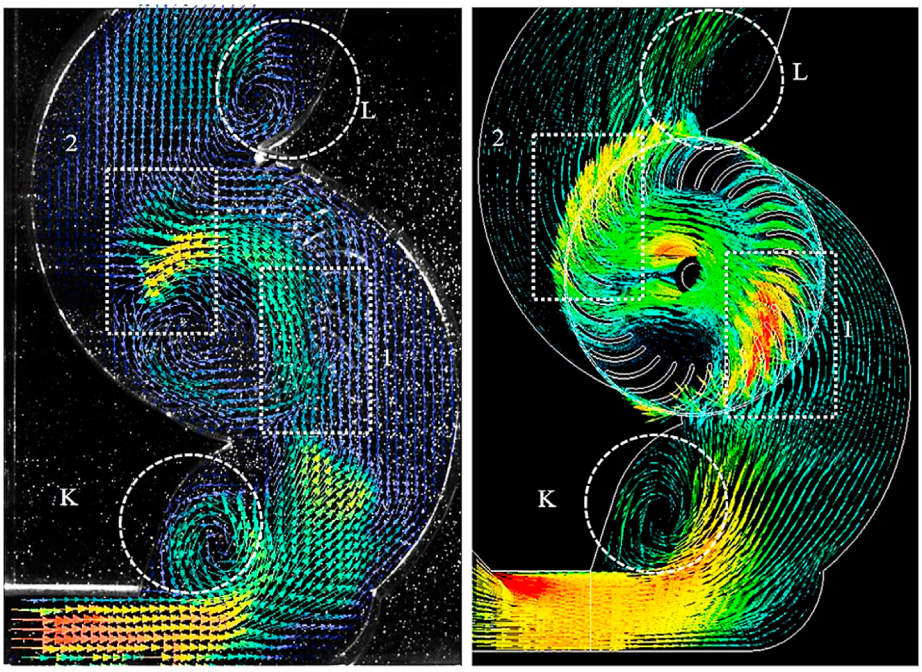

Fig. 24. Comparison of computational and experimental flow characteristics in the OWC for advancing flow.

$$P_t = \tau \times \omega \tag{12}$$

$$\eta_t = \frac{P_t}{P_{wave} \times W_G} \tag{13}$$

The turbine power output for varying wave heights and water depths for the wave period of 2.5 s is shown in Fig. 19. The turbine produces more power as the wave height increases for given water depths. This is expected since the incoming waves have higher energy with increasing wave heights and due to the higher input energy, the turbine produces more power. The next observation made from Fig. 19 is that the turbine produces more power at the water depth of 1.1 m compared to 0.8 m. The height of the guide nozzle at the inlet is approximately 0.8 m and at a water depth of 0.8 m, it is just submerged below the free surface. As the waves move towards the guide nozzle it was observed that the guide nozzle was not fully filled with water. This meant that the bulk movement of water did not impart momentum onto the turbine effectively. On the other hand, at the water depth of 1.1 m, the guide nozzle was always filled with water. The water was funneled towards the turbine effectively and hence imparted more energy to the turbine blades resulting in the generation of higher turbine power.

The turbine efficiencies for varying wave heights and water depths for the wave period of 2.25 s are shown in Fig. 20 against the rotational speed. Higher efficiencies are recorded for greater water depths, as expected. The results indicate that the turbine performance is highly dependent on the interaction of the waves with the rotor. The peak occurs at a wave height of 0.2 m instead of 0.25 m. The peaks indicate a resonance effect. It was generally observed that the efficiency increased with increasing wave period.

The maximum efficiency of 48.31% which corresponds to a turbine power of 13.2 W was recorded at the wave height, wave period, water depth and turbine rotational speed of 0.2 m, 2.75 s, 1.1 m and 35 rpm respectively, as shown in Fig. 21. It should be noted that under steady flow conditions, the maximum efficiency was recorded at 50 rpm, while under the action of waves that advance and recede, the turbine is likely to rotate at a lower rpm, which is what is observed in the present experiments. In addition, there were reflections of the waves to a small extent from the turbine (the flow that was not entering the blades), which caused some resistance to the rotation of the turbine and reduced its rotational speed.

3.3. Validation of computational results

For comparing the computational results with the experimental results in the present work as well as with previous works, the chosen wave height, wave period and water depth were 0.15 m, 2.50 s and 0.8 m respectively. The turbine efficiencies obtained through CFD and experiments at three turbine rotational speeds are shown in Fig. 22. The CFD code is able to predict the turbine performance with great accuracy. The average difference is around 3.75%. The CFD code slightly under-predicts the performance; a similar trend was observed by Prasad et al. [12].

The water oscillations in the rear chamber obtained from CFD and experiments were also compared as shown in Fig. 23. It can be seen that the trend and the values from CFD and experiments are similar and CFX is able to capture the oscillations very accurately. The comparisons shown in Figs. 22 and 23 validate the computational results with the experimental results and shows that the CFX results can be reliably used in this work.

The efficiencies achieved in the present work are compared with similar past works and the comparison is presented in Table 3. The efficiency recorded in the present study using a vertically configured augmentation channel compares well with its horizontal counterparts. The findings of the present work show that the vertically configured augmentation channel, which is more compact and occupies less space, can be used for wave energy extraction. Moreover, such a configuration can be used to extract

Table 3
Efficiency comparison between present work and similar past works.

Reference	Maximum Efficiency (%)	Comments
Prasad et al. [12]	55	Horizontally configured augmentation channel (fixed OWC)
Prasad et al. [13]	44.73	Horizontally configured augmentation channel (fixed OWC)
Choi et al. [14]	48.6	Horizontally configured augmentation channel (fixed OWC)
Kim et al. [16]	35–45	Horizontally configured augmentation channel (floating OWC)
Present work	**48.31**	**Vertically configured augmentation channel (fixed OWC)**

wave energy efficienctly at locations where the waves come predominantly from one direction.

Apart from comparing the turbine efficiencies and rear chamber water oscillations, the flow characteristics observed from CFD and PIV were also compared. The advancing flow into the augmentation channel is shown in Fig. 24. The blades receive the energy from the incoming flow at stage 1. The acceleration of the flow on the upper surface (suction) and the deceleration on the lower surface (higher pressure) of the blades results in part of the power generation due to the pressure difference on the two sides of the blades (clearly visible in Fig. 16). The water can be seen to accelerate as it exits the first stage blades and flows across towards the second stage blades. The water flowing out of the blade passage at stage 1 still possesses energy; the flow accelerates due to the convergent passages from the inlet to the outlet of the blades and again imparts energy to the blades at stage 2. The flow that passes through the blades at stage 1 and later through the blades at stage 2 is known as the cross-flow. The accelerated flow does not enter the blades at stage 2 tangentially. It strikes the blades at an angle and due to the resulting impulse, a force is exerted on the stage 2 blades. The water transfers some of its momentum to the blades [12,39]. The re-circulating flow in regions K and L had been also captured accurately by the CFD code. The vortex flow is generally attributed to the sharp corners present in the model. The retreating flow from the augmentation channel is shown in Fig. 25. The flow patterns observed in regions M, N and P are again accurately captured by CFD. Overall, the comparison of the flow characteristics from CFD and PIV shows very similar behavior. It can be observed from the results and the above discussion that the cross-flow turbine is the most appropriate turbine in this case since it rotates in the same direction irrespective of the direction of water flow and responds quickly to changes in the flow conditions at the same time avoiding any significant losses.

4. Conclusions

In the present work, the geometry of the augmentation channel, placed in a vertical orientation, was first optimized numerically using steady flow analysis. The optimized model had a curved bottom wall nozzle shape, curved upper-wall nozzle shape, 75 mm nozzle height and 45° front guide angle. The base model was numerically optimized using commercial CFD code ANSYS-CFX. The efficiency of the optimized model was 44.07% compared to the efficiency of 38.58% for the base model indicating an improvement in performance. These findings indicate that the performance of the turbine at fixed flow conditions can be improved by optimizing the various components of the augmentation channel which is on both sides of the turbine. The optimized model was then constructed for experimental work to be conducted in the wave channel and also simulated in NWT. The maximum efficiency was 48.31% obtained at a wave period of 2.75 s, a mean water depth of 1.1 m, and a wave height of 0.2 m at a turbine rotational speed of 35 rpm. The ideal operating range of the turbine was between 30 rpm and 40 rpm under the influence of waves' bi-directional flow. The optimized model when tested for waves using NWT and experimental conditions for bi-directional flow, the turbine efficiency boosted

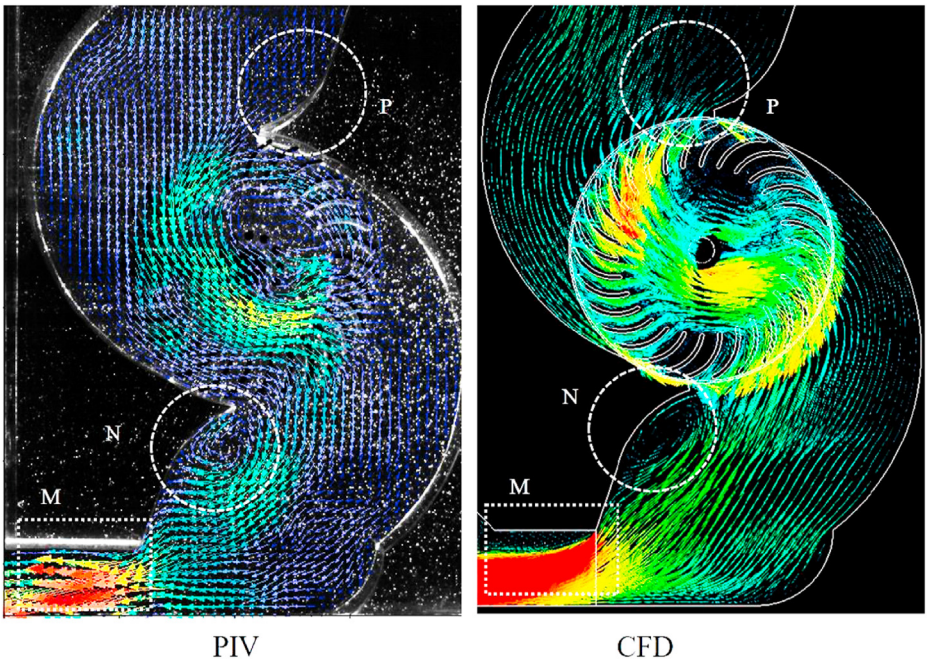

Fig. 25. Comparison of computational and experimental flow characteristics in the OWC for receding flow.

approximately by 4% which also proves that the novel vertical augmentation channel design is strongly suitable for bi-directional flows. It was observed from the results that the cross-flow turbine is the most appropriate turbine in this case since it ensures smooth entry of the flow to the turbine avoiding any significant losses. The efficiency increased with increasing wave period. PIV measurements were made to study the flow characteristics and also to compare the CFD results. The CFD code was able to predict the turbine performance accurately with an average deviation of 3.75%. In addition, the flow characteristics observed using CFD were similar to those observed experimentally using PIV. The optimized configuration can be used to efficiently harness wave energy.

Data availability

Sample data are attached with the submission. Other data will be made available upon request.

CRediT authorship contribution statement

A.H. Samitha Weerakoon: Formal analysis, optimization work. **Byung-Ha Kim:** Guidance for computational and experimental work in the lab., initial simulations. **Young-Jin Cho:** Transient flow simulations for . **Deepak Divashkar Prasad:** Investigation, finalizing testing conditions. **M. Rafiuddin Ahmed:** Writing – review & editing, discussion of results, finalization of manuscript. **Young-Ho Lee:** Conceptualization, project approval, Methodology, overall supervision of project.

Declaration of competing interest

The authors declare that they have no known competing financial interests or personal relationships that could have appeared to influence the work reported in this paper.

Appendix A. Supplementary data

Supplementary data to this article can be found online at https://doi.org/10.1016/j.renene.2021.08.092.

References

[1] R.G. Newell, D. Raimi, G. Aldana, Global Energy Outlook 2019: the Next Generation of Energy, 2019.
[2] T.F. Stocker, D. Qin, G.K. Plattner, M.M.B. Tignor, S.K. Allen, J. Boschung, A. Nauels, Y. Xia, V. Bex, P.M. Midgley (Eds.), IPCC 2013: Climate Change 2013 : the Physical Science Basis. Contribution of Working Group I to the Fifth Assessment Report of the Inter-governmental Panel on Climate Change, Cambridge University Press, New York, 2013, p. 1535.
[3] J. Vining, A. Muetze, Economic Factors and incentives for ocean energy conversion, IEEE Trans. Ind. Appl. 45 (2009) 547–554.
[4] N.N. Panicker, Power resource potential of ocean surface waves. Proceedings of the Wave and Salinity Gradient Workshop, 1976, pp. J1–J48.
[5] P. Halder, S.H. Rhee, A. Samad, Numerical optimization of wells turbine for wave energy extraction, International Journal of Naval Architecture and Ocean Engineering 9 (2017) 11–24.
[6] P. Halder, A. Samad, D. Thevenin, Improved design of a wells turbine for higher operating range, Renew. Energy 106 (2017) 122–124.
[7] Abdulhadi, R. O., The performance of 0.6 m impulse turbine operating under Bi-directional airflow. In: Proceedings of 2nd International Conference on Energy Systems and Technologies. Cairo, Egypt, 18-21 February, 2013.
[8] R. Badhurshah, A. Samad, J. Sangwai, Analysis of flow through ocean energy harvesting bidirectional impulse turbine, International Journal of Ocean and Climate Systems 5 (2) (2014) 51–63.
[9] Y. Luo, A. Presas, Z. Wang, Numerical analysis of the influence of design parameters on the efficiency of an OWC axial impulse turbine for wave energy conversion, Energies 12 (2019).
[10] A.F.O. Falcao, J.C.C. Henriques, Oscillating water columns wave energy converters and air turbines – a review, Renew. Energy 85 (2016) 1391–1424.
[11] J.J. Patel, T.B. Patel, D.A. Patel, Current status of wells turbine for wave energy conversion, International Journal for Scientific Research & Development 2 (11) (2015) 91–96.
[12] D.D. Prasad, M.R. Ahmed, Y.H. Lee, Flow and performance characteristics of a direct drive turbine for wave power generation, Ocean. Eng. 81 (2014) 39–49.
[13] Prasad, D., Ahmed, M. R. and Lee, Y. H., Performance studies on a direct drive turbine for wave power generation in a numerical wave tank. Proceedings of the 1st Asian Wave and Tidal Conference Series. Jeju Island, Korea, 27-30 November, 2012.
[14] Y.D. Choi, C.G. Kim, Y.T. Kim, J.I. Song, Y.H. Lee, A performance study on a direct drive hydro turbine for wave energy converter, J. Mech. Sci. Technol. 24 (11) (2010) 2197–2206.
[15] Y.D. Choi, C.G. Kim, Y.H. Lee, Effect of wave conditions on the performance and internal flow of a direct drive turbine, J. Mech. Sci. Technol. 23 (6) (2009) 1693–1701.
[16] B.H. Kim, J. Wata, M.A. Zullah, M.R. Ahmed, Y.H. Lee, Numerical and experimental studies on the PTO system of a novel floating wave energy converter, Renew. Energy 79 (2015) 111–121.
[17] H. Akimoto, K. Tanaka, Y. Kim, Drag-type cross-flow water turbine for capturing energy from the orbital fluid motion in ocean waves, Renew. Energy 76 (2015) 196–203.
[18] C. Windt, J. Davidson, J.V. Ringwood, High-fidelity numerical modelling of ocean wave energy systems: a review of computational fluid dynamics-based numerical wave tanks, Renew. Sustain. Energy Rev. 93 (2018) 610–630.
[19] ANSYS, Inc, ANSYS CFX-solver theory guide, available at, www.ansys.com, 2016.
[20] Y.J. Cho, A Study on the Flow Characteristics of a Direct Drive Turbine for Energy Conversion Generation Using Commercial CFD Code, Master's Thesis, Korea Maritime and Ocean University, Busan, South Korea, 2009.
[21] Y.J. Cho, Experimental and CFD Analysis of a Vertical Type Cross-Flow Turbine Design for Wave Power Generation, PhD Thesis. Korea Maritime and Ocean University, Busan, South Korea, 2017.
[22] Lui, Z., Hyun, B. S. and Hong K. Y., Application of numerical wave tank to OWC air chamber for wave energy conversion. In: Proceedings of the 18th International Offshore and Polar Engineering Conference. Vancouver, BC, Canada, 6-11 July, 2008.
[23] M.N. Gomes, C.R. Olinto, L.A.O. Rocha, J.A. Souza, L.A. Isoldi, Computational modeling of a regular wave tank, Therm. Eng. 8 (1) (2009) 44–50.
[24] S. Lais, Q. Liang, U. Henggeler, T. Weiss, X. Escalar, E. Egusquiza, Dynamic analysis of Francis runners - experiment and numerical simulation, International Journal of Fluid Machinery and Systems 2 (4) (2009) 303–314.
[25] D.D. Prasad, C.G. Kim, H.G. Kang, M.R. Ahmed, Y.H. Lee, Performance and flow characteristics of single and a novel double oscillating water column devices, J. Mech. Sci. Technol. 31 (12) (2009) 5879–5886.
[26] Choi, Y. D., Kim, C. G., Cho, Y. J., Kim, Y. T. and Lee, Y.H., Internal flow characteristics of cross flow hydraulic turbine for wave power system. In: Proceedings of the 9th Asian International Conference on Fluid Machinery. Jeju, South Korea, 16-19 October, 2007.
[27] J. Twidell, T. Weir, Renewable Energy Resources, third ed., Routledge, 2015.
[28] R.G. Dean, R.A. Dalrymple, Water Wave Mechanics for Engineers and Scientists, World Scientific Publishing, Singapore, 2010.
[29] N. Acharya, C.G. Kim, B. Thapa, Y.H. Lee, Numerical analysis and performance enhancement of a cross flow hydro turbine, Renew. Energy 80 (2015) 819–826.
[30] H.G.S. Totapally, N.M. Aziz, Refinement of cross-flow turbine design parameters, J. Energy Eng. 120 (1994) 133–147.
[31] Z. Chen, P.M. Singh, Y.D. Choi, Effect of guide nozzle shape on the performance improvement of a very low head cross flow turbine, The KSFM Journal of Fluid Machinery 17 (5) (2014) 19–26.
[32] R. Adhikari, D. Wood, A new nozzle design methodology for high efficiency crossflow hydro turbine, Energy for Sustainable Development 41 (2017) 139–148.
[33] R. Adhikari, D. Wood, The design of high efficiency crossflow hydro turbines: a review and extension, Energies 11 (2018) 267.
[34] A. Zaffar, B. Ibrahim, M.A. Sarwar, J.A. Chattha, M. Asif, Optimisation of blade profiles of cross flow turbine, Int. J. Power Energy Convers. 9 (4) (2018) 311–326.
[35] Y.C. Ceballos, M.C. Valencia, D.H. Zuluaga, J.S.D. Rio, S.V. Garcia, Influence of the number of blades in the power generated by a michell banki turbine, International Journal of Renewable Energy Research 7 (4) (2017) 1989–1997.
[36] V. Sammartano, C. Arico, A. Carravetta, O. Fecarotta, T. Tucciarelli, Banki-michell optimal design by computational fluid dynamics testing and hydrodynamic analysis, Energies 6 (2013) 2362–2385.
[37] A.H. Elbatran, O.B. Yaakob, Y.M. Ahmed, M.R. Jalal, Novel approach of bidirectional diffuser-augmented channels system for enhancing hydrokinetic power generation in channels, Renew. Energy 83 (2015) 809–819.
[38] G. Mehr, M. Durali, M.H. Khakrand, H. Hoghooghi, A novel design and performance optimization methodology for hydraulic cross-flow turbines using successive numerical simulations, Renew. Energy 169 (2021) 1402–1421.
[39] K.P. Kim, M.R. Ahmed, Y.H. Lee, Efficiency improvement of a tidal current turbine utilizing a larger area of channel, Renew. Energy 48 (2012) 557–564.